

## 仿生超疏水表面在微夹持器钳口端面的应用研究

杨成娟<sup>1,2</sup>, 杨雪<sup>1,2\*</sup>, 王蒙<sup>1,2</sup>, 王福军<sup>1,2</sup>, 时贝超<sup>1,2</sup>, 朱鑫垚<sup>1,2</sup><sup>1</sup>天津大学机械工程学院, 天津 300072;<sup>2</sup>天津大学机械工程学院机构理论与装备设计教育部重点实验室, 天津 300072

**摘要** 微夹持器是微操作系统的重要组成部分。作为微操作系统末端执行器,微夹持器钳口端面在工作过程中容易出现磨损、吸附杂质、结冰或结霜等问题,而且目前微夹持器大多是一体化加工而成,整体更换将造成资源浪费。本文设计了一种可拆卸式微夹持器,利用中心波长为 1064 nm 的纳秒激光器,在执行操作的钳口端面上加工出粗糙的微纳结构,使用无毒害的硬脂酸溶液浸泡改性,获得仿生超疏水表面。通过电化学实验,测试了仿生超疏水表面在酸、盐和碱环境中的耐腐蚀性能,通过自清洁、抗结冰和抗菌实验测试了该表面的防污、防冻和抗菌性能。实验结果表明:仿生超疏水表面能够有效抵抗酸、盐和碱环境中的腐蚀,具有良好的防腐性能;有效防止灰尘、水滴和细菌等杂质粘附于钳口端面,保证钳口端面的清洁与卫生;在低温环境中,有效防止端面结霜或结冰,使微夹持器能够在恶劣环境中正常工作。

**关键词** 激光技术; 表面加工; 仿生超疏水表面; 微夹持器; 耐腐蚀; 自清洁; 抗结冰; 抗菌

**中图分类号** TN249

**文献标志码** A

**DOI:** 10.3788/CJL202249.1002602

## 1 引言

自然界中一些植物和昆虫因其表面特殊微/纳米级粗糙结构和低表面能物质,表现出特殊的湿润性<sup>[1-2]</sup>。例如:荷叶的超疏水自清洁性能是通过微米级的乳突结构和分布在乳突上凸起的纳米结构共同作用实现的<sup>[3-5]</sup>;水稻稻叶微观上具有波纹状结构,波纹状结构上分布着纳米级颗粒,其表面具有超疏水特性的同时也具有各向异性<sup>[6-8]</sup>;鲨鱼发展出带有微米沟槽状结构的皮肤来抵抗细菌细胞的附着<sup>[9-11]</sup>;蝉和蜻蜓翅膀的穗状纳米结构可以杀死几种致病细菌<sup>[12-14]</sup>。受此启发,许多研究人员通过研究这些动植物的表面微观结构,设计并制备出仿生超疏水表面,这些表面因具有自洁、防冰、减阻、抗腐蚀等优良特性,在工业、军事、生物医学等领域具有巨大的应用价值<sup>[15-20]</sup>。

微夹持器作为微操作系统的末端执行器,直接与被操作物体接触并完成对被操作物体的相关操

作,其工作精度与稳定性对操作系统的性能有着至关重要的影响<sup>[21-26]</sup>。目前,传统的微夹持器大多是一体化加工成型,为了实现精密操作,通常两个夹钳钳口端面之间的距离大约只有 0.5 mm,夹持对象仅有几十至几百微米。然而,微夹持器的夹钳在执行操作的过程中受到环境污染,导致其钳口端面出现腐蚀、吸附杂质和粘附细菌等现象,在寒冷环境中容易出现结冰和结霜的问题,导致夹钳局部受损,而两个夹钳钳口端面之间的距离设计得如此微小,无法对钳口端面进行表面处理来进一步提高其抗腐蚀、防污、抗冰、抑菌等性能。此外,一体化的微夹持器无法对局部受损的夹钳进行更换,只能采取整台报废的处理措施,这将造成人力和资源的浪费。传统钳口端面的摩擦系数小、黏附力大,在执行操作过程中难以夹取和释放物体,从而影响微夹持器的正常使用性能。因此,克服微夹持器夹钳存在的上述问题,提高微夹持器的使用性能与服役寿命,近年来受到了越来越多人的关注<sup>[27-31]</sup>。

**收稿日期:** 2021-12-27; **修回日期:** 2022-02-01; **录用日期:** 2022-02-28

**基金项目:** 国家重点研发计划—政府间国际科技创新合作重点专项(2017YFE0112100)、国家重点研发计划(2017YFB1104700)

**通信作者:** \* xue\_yang@tju.edu.cn

针对传统微夹持器存在的诸多问题,本文设计并制作了一种可拆卸式仿生超疏水微夹持器。首先,利用可拆卸式模块化设计方案在夹持对象、操作环境与夹钳钳口端面样式之间建立映射关系,为提高微夹持器的柔性及灵活性、延长其整机使用寿命做出积极的探索。其次,在两个夹钳的钳口端面制作出超疏水表面,并对超疏水表面进行防腐、防污、抗冰和抑菌性能测试。通过在不同 pH 值下进行腐蚀实验,对比超疏水表面在酸、盐和碱环境中的耐腐蚀性能;利用固结冰的附着量来评估其防结冰性能<sup>[32]</sup>;采用自主设计的自清洁实验验证其防污性能;通过激光共聚焦显微镜观察细菌分布与存活情况,并进行平板涂布实验计算抑菌率,表征其抗菌性能。

## 2 仿生超疏水微夹持器的设计及制作

### 2.1 微夹持器的机械结构设计

根据具体的夹持对象和操作环境选用适宜的

夹钳可以提高微夹持器的使用灵活性,因此将传统一体化成型的微夹持器进行拆分设计,并根据实际需求在夹钳的钳口端面上制作不同的功能表面,使夹钳模块化,这种设计能够延长其整机的使用寿命。本实验在夹钳钳口端面设计的功能表面具有仿生超疏水结构,这种仿生超疏水表面能够降低夹钳钳口端面的黏附力,同时具有耐腐蚀、自清洁、抗结冰和防菌等性能。图 1 所示为具有仿生超疏水结构的可拆卸式微夹持器的设计模型,其整体划分为上、下两个部分:第一部分是具有柔性机构的基体;第二部分是与基体相连的左夹体和右夹体,两个夹体通过螺栓对称地固定在基体上,左夹体和右夹体的执行末端钳口端面加工有微米级网格结构。

### 2.2 仿生超疏水钳口端面的制作

图 2 为基于图 1 所示微夹持器模型的实物图,左、右夹体的钳口端面尺寸为 3 mm×1 mm,夹持

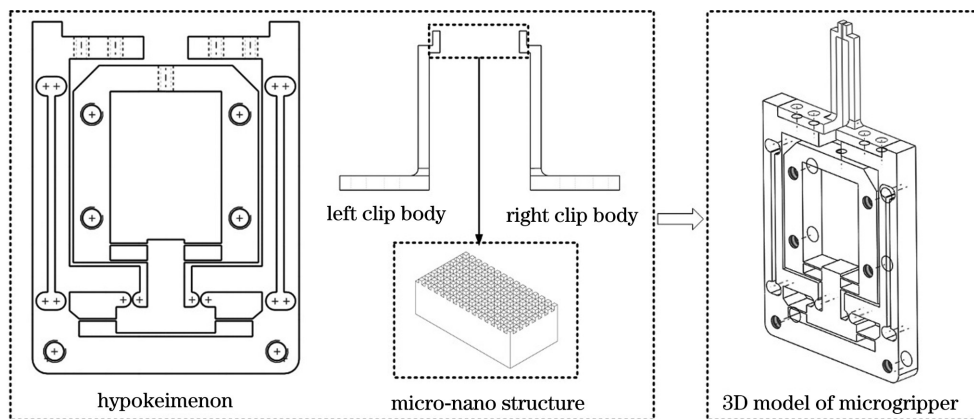


图 1 具有仿生超疏水结构的可拆卸式微夹持器模型

Fig. 1 Model of detachable microgripper with bionic superhydrophobic structure

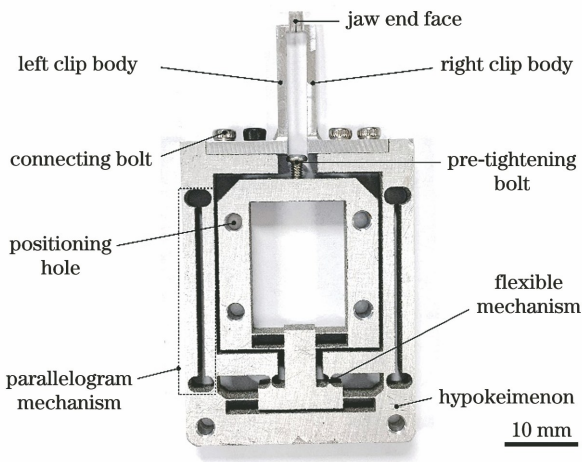


图 2 微夹持器实物图

Fig. 2 Physical picture of microgripper

间距为 0.5 mm。在模仿动植物表面的微观结构时,使用纳秒脉冲激光在微夹持器左、右两个夹体的钳口端面制备仿生微观结构,随后辅以硬脂酸  $[\text{CH}_3(\text{CH}_2)_{16}\text{COOH}]$  溶液浸泡,使其表面获得超疏水特性。

#### 2.2.1 激光加工系统

采用纳秒光纤激光器(德国 IPG Photonics 公司)按照预定加工路径制备具有特殊纹理样式的微结构表面。这台激光器可以发射 1064 nm 中心波长的脉冲,重复频率为 20 kHz,持续时间为 50 ns。纳秒激光加工系统和激光扫描路径如图 3 所示,将制备好的样品置于加工平台上。激光光束沿光路传输,最终以直径为 50 μm 的聚焦光斑垂直入射到样品表面。激光功率为 16 W,扫描速度为

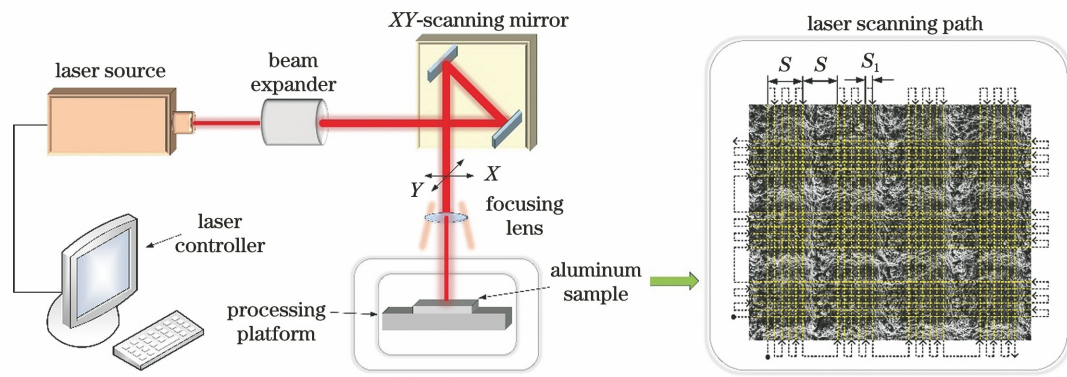


图 3 纳秒激光加工系统和激光扫描路径示意图

Fig. 3 Schematic of nanosecond laser processing system and laser scanning path

500 mm/s, 激光光束按照预设的路径在两个垂直方向上逐行扫描烧蚀样品表面, 其中  $S_1 = 20 \mu\text{m}$ ,  $S = 100 \mu\text{m}$ , 如此循环往复, 形成网格状微结构阵列。

### 2.2.2 加工步骤

夹持器材料为 7075 铝, 首先使用金相试样研磨抛光机对样品进行打磨(先利用 800 目的砂纸粗磨, 再利用 2000 目的砂纸精磨), 使端面的粗糙度  $R_a$  降低到  $1.5 \mu\text{m}$  以下; 然后使用乙醇溶液、蒸馏水依次对样片进行超声洗涤 10 min, 以去除表面污物, 清洗后将样品放置在烘干箱中进行干燥处理, 除去水分。使用纳秒激光器刻蚀样品表面制备网格状微结构, 得到初始的激光加工表面, 然后将样品置于无毒害的浓度为  $0.05 \text{ mol/L}$  的硬脂酸溶液中浸泡 30 min 以降低表面自由能<sup>[33]</sup>, 取出后将其置于  $60 \text{ }^\circ\text{C}$  烘干箱中烘干 1 h, 至此, 样品表面制备完成, 待后续进行分析与验证。图 4 所示为制备得到的功能化钳口端面与原始钳口端面的实物对比。

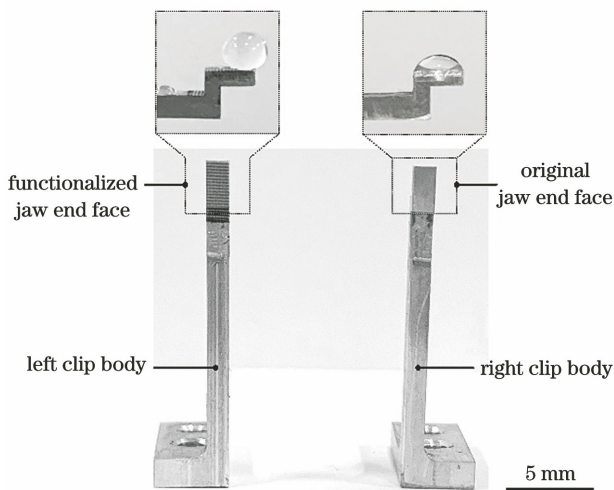


图 4 功能化钳口端面和原始钳口端面的实物对比

Fig. 4 Physical comparison of functionalized jaw end face and original jaw end face

## 3 超疏水表面性能测试

为方便后期观察、测试与分析, 选用尺寸为  $10 \text{ mm} \times 10 \text{ mm}$ 、厚度为  $1 \text{ mm}$  的 7075 太空铝片代替钳口端面进行性能测试。将清洗干燥后未经任何处理的铝样品记作 Al-I, 经纳秒激光烧蚀和硬脂酸溶液浸泡并干燥后得到的铝样品记作 Al-II。使用接触角测量仪(VCA optima, AST)测量样品表面的接触角, 使用接触角测量仪(SZ-CAMC33)测量样品表面的滚动角, 通过计算机控制软件, 控制液滴体积为  $6 \mu\text{L}$ , 在同一个样品的 3 个不同位置进行接触角和滚动角测量, 各测试 3 个相同样品。通过测量得到 Al-I 样品的接触角平均值为  $59.6^\circ$ , 滚动角均大于  $90^\circ$ , Al-II 样品的接触角平均值为  $156.7^\circ$ , 滚动角平均值为  $1.088^\circ$ , 说明所制备的 Al-II 样品表面均具备优异的超疏水性能。此外, 还测试了 Al-II 样品置于空气中 30 天后的接触角和滚动角, 其平均值分别为  $155.1^\circ$  和  $4.908^\circ$ , 说明利用所提方法制备得到的超疏水样品具有良好的稳定性。

针对微夹持器的功能需求, 对所获得的超疏水 Al-II 样品表面分别进行耐腐蚀、自清洁、抗结冰和抗菌性能测试。使用 X 射线光电子能谱仪(XPS, Thermo Fischer, SCALAB 250Xi)检测 Al-I 和 Al-II 表面的化学成分; 利用扫描电子显微镜(SEM, TESCAN MIRA4)表征 Al-I 和 Al-II 样品经酸、碱、盐腐蚀前、后的表面形貌; 采用环境试验箱(DHTC-27-40-P-SD)和自主设计的自清洁实验评估 Al-I 和 Al-II 样品的抗结冰与自清洁性能; 使用激光共聚焦显微镜(Olympus FV1200)表征 Al-I 和 Al-II 样品表面的细菌分布及存活状况。

### 3.1 化学成分

采用 XPS 对原始样品 Al-I 和超疏水样品

Al-II 进行表面化学成分分析,结果如图 5(a)、(b) 所示。两种样品表面的 XPS 电子能谱都包含 3 种元素:C (位于 284.7 eV 的 C 1s)、O (位于 531.7 eV 的 O 1s)和 Al (位于 74.7eV 的 Al 2p),其中 Al 2p 为 O—Al—O 键合,从图 5(b) 的 C 1s 核级谱可以看出,激光照射后 O 的原子数分数上升到 24.51%,这是因为激光照射过程中生成了氧化铝( $\text{Al}_2\text{O}_3$ )。与图 5(c)所示的原始样品 Al-I 的 C 1s 高分辨率光谱相比,图 5(d)所示的 C 1s 高分辨率光谱显示经硬脂酸溶液改性处理后 C 含量明显增加,表明在化学改性过程中,硬脂酸与表面的铝反应生成具有

低表面能的硬脂酸铝<sup>[34]</sup>。为了进一步确定所制备超疏水表面的化学组成,图 5(d)给出了 C 1s 高分辨率光谱的 4 个峰值分量,位于 284.5, 285.7, 286.3, 288.3 eV 的峰信号分别来自 C—C(H)、C—O、C=O 和 O=C—O 的官能团<sup>[35]</sup>,其中 C—C(H)均占据最强的峰,C 的原子数分数高达 82.81%,表明硬脂酸的长链分子已经成功地以硬脂酸铝的形式粘附在所制备的超疏水 Al-II 表面。O=C—O 官能团存在于吸收的硬脂酸中,C—O 和 C=O 的极性部分可能来自清洗样品的乙醇残留物<sup>[36]</sup>。

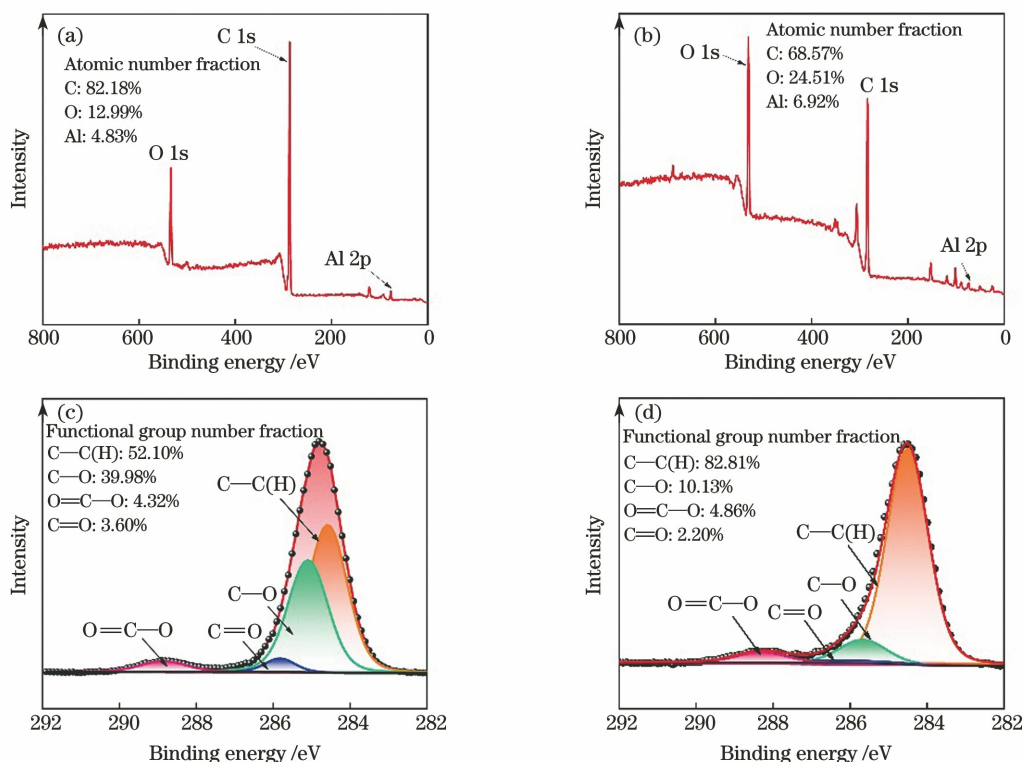


图 5 测量得到的 XPS 和 C 1s 高分辨率光谱。(a)Al-I 和(b)Al-II 样品的 XPS; 利用(c)Al-I 和(d)Al-II 样品的峰拟合得到的 C 1s 高分辨率光谱

Fig. 5 Measured XPS and C 1s high-resolution spectra. XPS of (a) Al-I and (b) Al-II samples; C 1s high-resolution spectra fitted by the spectrum peaks of (c) Al-I and (d) Al-II samples

### 3.2 耐腐蚀

腐蚀是一个严重且普遍的问题,它可能导致效率降低、产品污染甚至失效、工厂停工、资源浪费及环境破坏等<sup>[37]</sup>。超疏水表面能够最大限度地减少液体和表面之间的接触面积,提供极佳的耐腐蚀性能,因此在改善金属防腐蚀特性方面具有巨大的应用潜力<sup>[37-42]</sup>。腐蚀实验使用计算机控制的电化学工作站(CHI660D, CH Instruments, Inc.),在酸(pH=2 的 HCl)、盐(pH=7、质量分数为 3.5% 的 NaCl)和碱(pH=12 的 NaOH)溶液中进行。利用

动电位极化技术和强电化学阻抗谱(EIS)定量评价腐蚀行为<sup>[43]</sup>。分别将 Al-I 和 Al-II 作为工作电极,且控制其在电解液中暴露的面积为  $1 \text{ cm}^2$ 。采用在电解液中暴露面积为  $1 \text{ cm}^2$  的铂片作为辅助电极,并使用商业化硫酸亚汞电极( $\text{Hg}_2\text{SO}_4$ )、饱和甘汞电极(SCE)和双盐桥氧化汞电极( $\text{HgO}$ )分别作为酸、盐和碱环境中的参比电极。极化测试以  $10 \text{ mV/s}$  的扫描速率开展,EIS 测量在  $0.01 \sim 100000 \text{ Hz}$  的频率范围内进行,正弦波扰动为  $10 \text{ mV}$ ,Al-I 和 Al-II 样品每 10 倍频记录 12 点。

EIS 实验结果通过 ZSimPWin 软件进行数据分析, 拟合等效电路<sup>[44]</sup>。

图 6 为 Al-I 和 Al-II 两种样品经酸、盐和碱溶液腐蚀前、后的 SEM 图, 总体来说, 经酸、盐和碱溶液腐蚀后 Al-I 表面均出现了大面积的腐蚀区域, 而 Al-II 表面仅有较小区域被腐蚀。对比图 6(b)、(f) 发现, 经酸性溶液腐蚀后两种表面均有新物质附着, 这可能是因为 Al 和 HCl 发生反应生成 AlCl<sub>3</sub>;

图 6(h) 显示经碱腐蚀后 Al-II 表面出现大量因点蚀形成的凹坑, 相比之下, 图 6(g) 则显示经盐溶液腐蚀后 Al-II 表面仅有少量的腐蚀坑存在, 说明超疏水表面在盐溶液中的抗腐蚀性能要优于其抗酸、碱的性能。腐蚀区域的产生是因为 Al 与强酸和强碱发生反应, 相应的方程式如下:

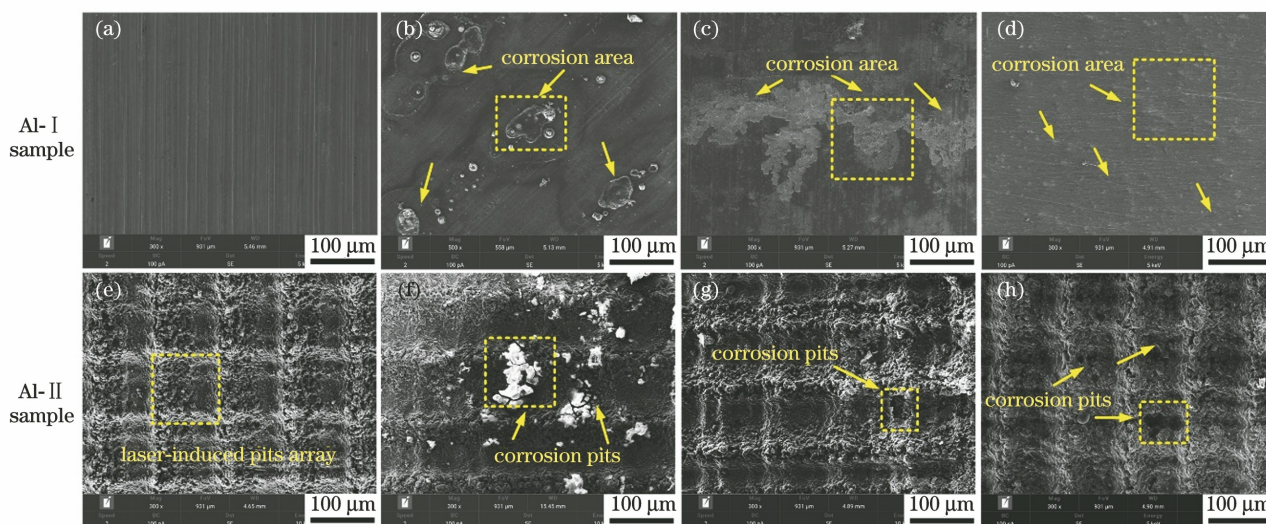
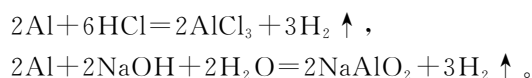


图 6 Al-I 和 Al-II 样品在酸、盐和碱溶液中的腐蚀情况对比。(a)(e) 未经腐蚀的样品; (b)(f) 经 pH=2 的 HCl 溶液腐蚀的样品; (c)(g) 经 pH=7 的 NaCl 溶液腐蚀的样品; (d)(h) 经 pH=12 的 NaOH 溶液腐蚀的样品

Fig. 6 Comparison of corrosion of Al-I and Al-II samples in acids, salts, and alkali solutions. (a)(e) Uncorroded samples; (b)(f) samples corroded by HCl solution at pH=2; (c)(g) samples corroded by NaCl solution at pH=7; (d)(h) samples corroded by NaOH solution at pH=12

Al-I 和 Al-II 样品在 pH=2、pH=7 和 pH=12 溶液中的极化曲线如图 7 所示, 根据 Tafel 外推法<sup>[34]</sup>, 阴极斜率( $\beta_c$ )和阳极斜率( $\beta_a$ )交点的横、纵坐标分别代表腐蚀电位( $E_{\text{corr}}$ )和腐蚀电流密度( $I_{\text{corr}}$ ), 极化电阻( $R_p$ )根据 Stern-Geary 公式计算

得到:

$$R_p = \frac{\beta_a \times \beta_c}{2.303 I_{\text{corr}} (\beta_a + \beta_c)} \quad (1)$$

表 1 所示的腐蚀参数表明, 在酸、盐和碱溶液中, 超疏水 Al-II 样品的腐蚀电流均小于原始 Al-I 样品, 超疏水 Al-II 样品的极化电阻均比原始 Al-I 样品高出约一个数量级, 说明所制备的超疏水表面能够显著提高铝基金属的抗腐蚀能力。

通过 EIS 测量, 进一步评估两种样品在酸、盐和碱溶液中的腐蚀性能。图 8 所示为 Al-I 和 Al-II 样品的电化学阻抗谱。图 8(a)~(c) 所示的奈奎斯特(Nyquist)曲线表明, 超疏水 Al-II 样品的电容环均高于原始 Al-I 样品, Nyquist 曲线中电容环的半圆直径表示样品表面和腐蚀介质之间的界面上形成的双层电荷转移电阻<sup>[34]</sup>, 直径越大意味着腐蚀速率越低, 说明相比原始样品, 超疏水样品在酸、盐和碱溶液中均具有良好的抗腐蚀性能。图 8(a)、(b) 中放大的 Nyquist 曲线表明: 在 pH=2 的 HCl

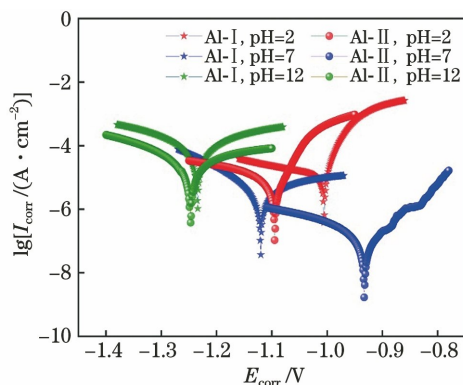


图 7 Al-I 和 Al-II 样品在 pH=2、pH=7 和 pH=12 溶液中的极化曲线

Fig. 7 Polarization curves of Al-I and Al-II samples in pH=2, pH=7, and pH=12 solutions

表 1 通过极化曲线得到的 Al-I 和 Al-II 样品在不同溶液中的腐蚀结果

Table 1 Corrosion results of Al-I and Al-II samples in different solutions obtained by polarization curves

Sample	$E_{\text{corr}} / \text{V}$	$I_{\text{corr}} / (\text{A} \cdot \text{cm}^{-2})$	$\beta_a / (\text{V} \cdot \text{dec}^{-1})$	$-\beta_c / (\text{V} \cdot \text{dec}^{-1})$	$R_p / (\Omega \cdot \text{cm}^2)$
Al-I (pH=2)	-1.01	$5.32 \times 10^{-5}$	0.13	0.30	$7.30 \times 10^2$
Al-II (pH=2)	-1.10	$1.26 \times 10^{-5}$	0.10	0.27	$2.52 \times 10^3$
Al-I (pH=7)	-1.12	$5.14 \times 10^{-6}$	0.30	0.11	$6.85 \times 10^3$
Al-II (pH=7)	-0.93	$1.62 \times 10^{-6}$	0.10	0.19	$1.79 \times 10^4$
Al-I (pH=12)	-1.23	$1.24 \times 10^{-4}$	0.22	0.19	$3.55 \times 10^2$
Al-II (pH=12)	-1.25	$3.78 \times 10^{-5}$	0.29	0.16	$1.18 \times 10^3$

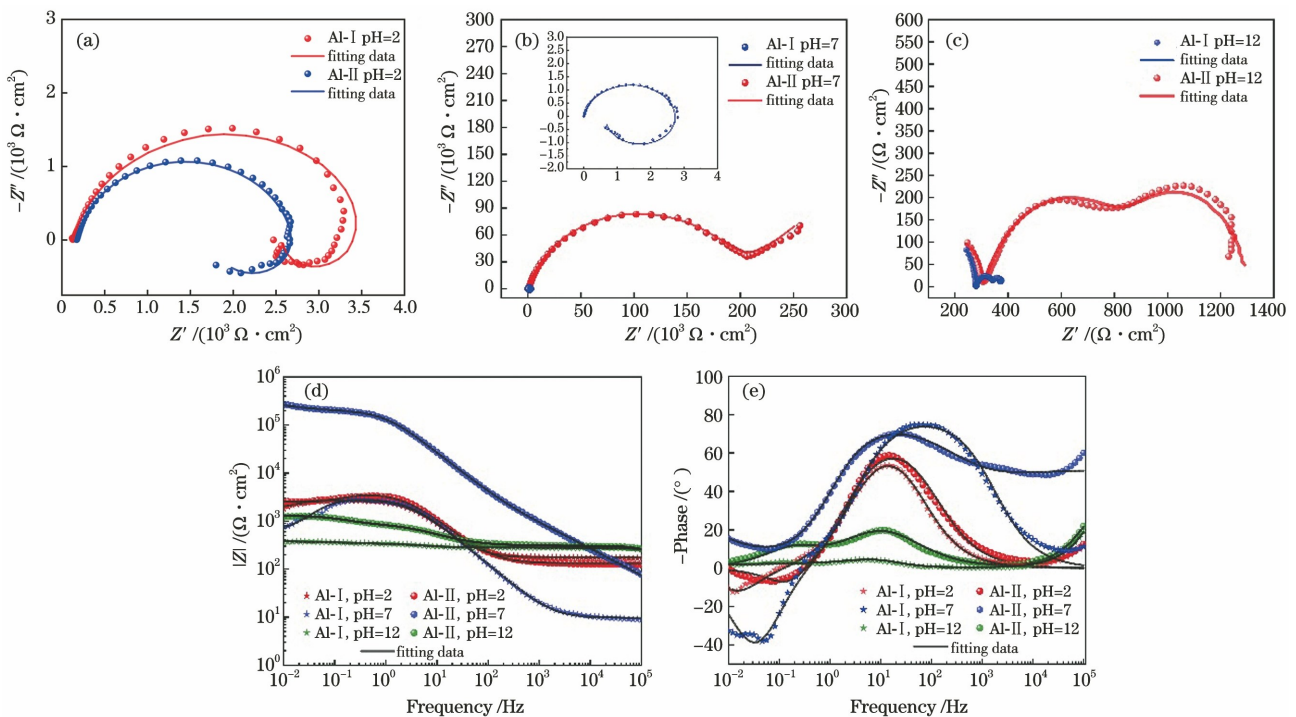


图 8 Al-I 和 Al-II 样品的电化学阻抗谱和极化曲线对比。(a) pH=2、(b) pH=7 和 (c) pH=12 溶液中样品的 Nyquist 图和拟合曲线；(d) 阻抗模量与频率的 Bode 图和拟合曲线；(e) 相位角与频率的 Bode 图和拟合曲线

Fig. 8 Comparison of electrochemical impedance spectra and polarization curves of Al-I and Al-II samples. Nyquist plots of samples in solutions with (a) pH=2, (b) pH=7, and (c) pH=12; (d) Bode diagram and fitting curves of impedance modulus and frequency; (e) Bode diagram and fitting curves of phase angle and frequency

溶液中,两种样品均在中高频范围显示电容环路,在低频范围显示电感回路;而在 pH=7 的 NaCl 溶液中,Al-I 样品具有相同的表现。通过研究发现,电容环的存在可能与电荷转移反应有关,电感回路可能与铝溶解导致的点蚀有关,低频范围尾部的存在表明铝基底上的硬脂酸涂层容易被损坏,然后裸露的铝层暴露在电解液中,导致腐蚀离子通过产生的凹坑渗透到基底中。图 8(b) 表明,超疏水 Al-II 样品具有最大的电容环,并且在低频范围内没有观察到电感环,说明在盐溶液中,超疏水涂层可以有效地保护裸露的铝表面,特别是避免点蚀。通过低频

下的伯德(Bode)阻抗模量对样品的腐蚀抑制性能进行评估,结果如图 8(d) 所示。较高的阻抗模量值表示样品具有较好的腐蚀抑制性能。显然,超疏水 Al-II 样品的总阻抗模量大于原始 Al-I 样品,这意味着具有多孔微结构的超疏水涂层可以显著增强铝材料的缓蚀性能。此外,图 8(e) 所示的 Bode 相位图表明,在酸和盐溶液中的 Al-I 样品,其低频相位角都小于  $0^\circ$ ,再次证明了电化学过程中会出现点蚀<sup>[45]</sup>。由此可见,Bode 和 Nyquist 结果均与极化曲线结果一致,充分证明了超疏水表面具有优异的缓蚀性能。图 9 为 Al-I 和 Al-II 样品 EIS 曲线对应

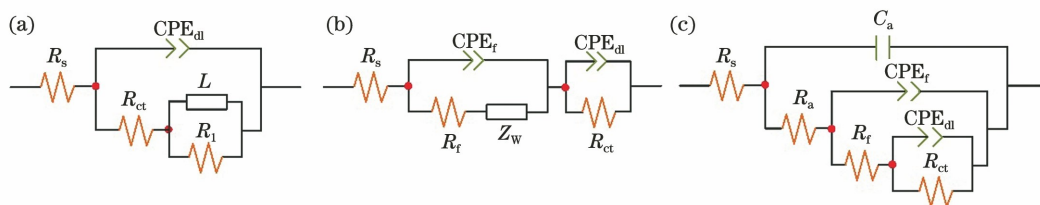


图 9 EIS 曲线的等效电路。(a) pH=2 时 Al-I、Al-II 表面和 pH=7 时 Al-I 表面；(b) pH=7 时 Al-II 表面；(c) pH=12 时 Al-I 表面和 Al-II 表面

Fig. 9 Equivalent circuit of EIS curves. (a) Al-I and Al-II surfaces at pH=2 and Al-I surface at pH=7; (b) Al-II surface at pH=7; (c) Al-I surface and Al-II surface at pH=12

的等效电路图,其中  $R_s$  表示样品和参比电极之间的电解质电阻,  $R_a$  和  $C_a$  表示截留在多孔微结构内的气穴的电阻和电容,  $L$  和  $R_l$  表示电感和相关电阻,用于分析低频下的电感回路,该回路源自电极上由于点蚀而解吸的物质<sup>[45]</sup>。  $R_{ct}$  表示样品表面和盐溶液的界面处形成的双层电荷转移电阻, CPE 表示恒定相位元件,用于改善拟合的阻抗数据<sup>[34]</sup>,  $Z_w$  表示韦伯阻抗,由一个扩散电阻  $R_w$  和一个扩散电容  $C_w$  串联组成。

### 3.3 自清洁

荷叶以其“自洁”能力而闻名,落在荷叶表面的水滴成珠、滚落,从而带走污染颗粒<sup>[46]</sup>。将这种“荷叶效应”所具有的自清洁特性应用于微夹持器的钳口端面,能够获得一种非常理想的微操作能力,对于那些暴露在多尘环境中的微夹持器钳口端面,滚水

除尘(如雨滴除尘)是一种高效、节能的表面清洁方法<sup>[47]</sup>。本实验以碳粉和粉笔末代表日常环境中的污染物,以 PVP 和  $Fe_2(NO_3)_3$  的混合粉末代表化学环境中的污染物,测试原始 Al-I 样品和超疏水 Al-II 样品表面的自清洁性能。将具有污染物的样品置于倾斜角度为  $15^\circ$  的工作平台上,如图 10(a)、(d)、(g)、(j)、(m)、(p) 所示;使用接触角测量仪(SZ-CAMC33)控制液滴体积为  $10 \mu L$ ,液滴在无外力的作用下,通过针管滴落在样品表面的上端,如图 10(b)、(e)、(h)、(k)、(n)、(q) 所示;液滴完全释放后与污染物接触,在 Al-I 样品表面短距离滑动后滞留[图 10(c)、(f)、(i)],而在 Al-II 样品表面液滴快速滚落至样品的下端,并带走表面的污染物,在表面留下清洁的痕迹[图 10(l)、(o)、(r)]。

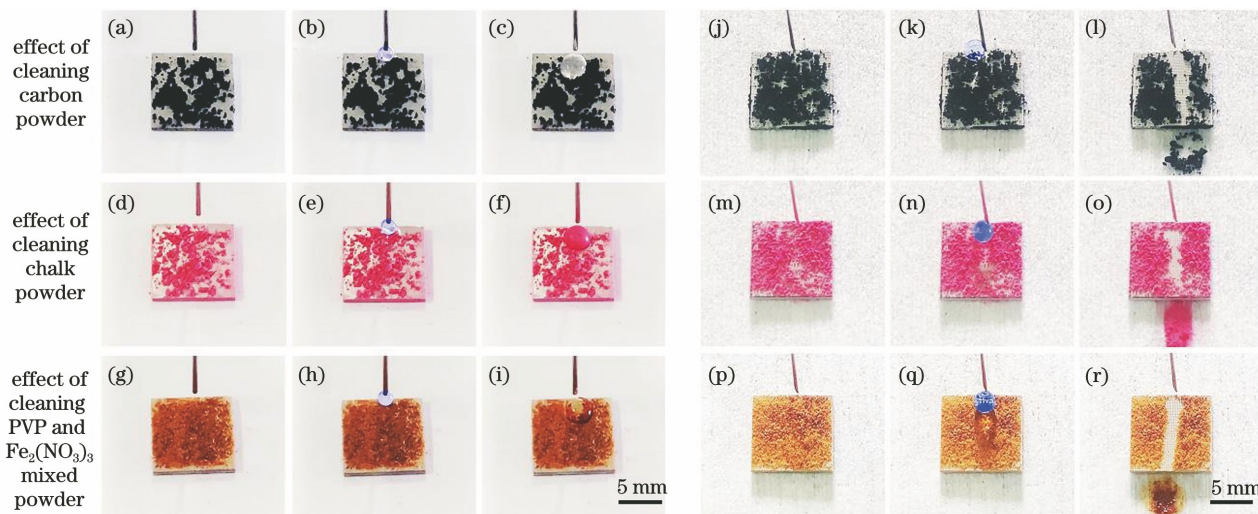


图 10 Al-I 和 Al-II 样品表面的自清洁效果对比,比例尺均为 5 mm。(a)~(i) Al-I 样品;(j)~(r) Al-II 样品

Fig. 10 Comparison of self-cleaning effects of Al-I and Al-II sample surfaces, both at a scale of 5 mm.

(a)~(i) Al-I sample; (j)~(r) Al-II sample

### 3.4 抗结冰

在低温环境中,传统微夹持器的钳口端面容易出现结冰、结霜现象,导致微夹持器出现故障并造成经济损失。因此,研制一种仿生超疏水表面来防止冷表面结冰和结霜是非常必要的<sup>[48]</sup>。本实验通过

固结冰的附着量来验证<sup>[32]</sup>,为便于实验现象观测,本实验采用  $30 \text{ mm} \times 30 \text{ mm} \times 1 \text{ mm}$  的 7075 铝样品片进行测试。首先将样品置于倾斜角度为  $25^\circ$  的实验平台上,利用环境试验箱控制样品表面和环境温度为  $-6^\circ \text{C}$ ,然后将温度为  $0^\circ \text{C}$  的水加入样品表面

正上方 2.5 cm 处的容器中,水滴通过容器下端的细管竖直滴落到样品表面,其实验装置如图 11(a)所示,水滴滴落到原始 Al-I 和超疏水 Al-II 样品表面的时长均为 20 min。图 11(b)~(s) 给出了原始 Al-I 和超疏水 Al-II 样品在不同时刻的结冰和防冰情况,以及水滴下落至样品表面并堆积或滚落的全部过程。可以清楚地看到,原始 Al-I 样品表面被温度为 0 °C 的水滴润湿,导致在 -6 °C 的环境温度

中短时间内快速结冰。经过 20 min 的测试时间后,Al-I 样品表面大部分被逐层堆积形成的厚冰覆盖,经称重黏附冰层的质量为 1.283 g,在低温环境中表现出较差的防结冰性能。相反,受益于优异的超疏水性能与低黏附能力,Al-II 样品表面和水滴之间接触面积积极小,水滴在重力作用下能够在结冰前迅速(接触时间极短)滚离样品表面,且基本无残留,因此在测试过程中没有明显结冰现象发生。

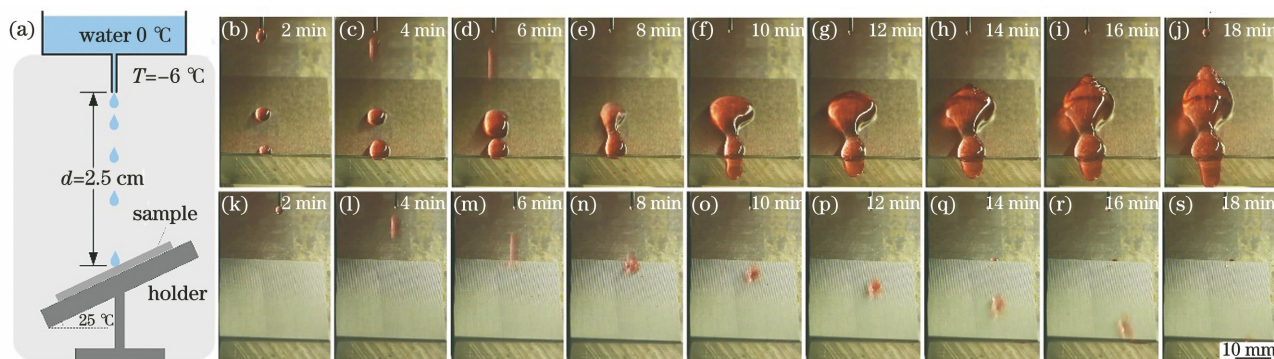


图 11 7075 铝样品的防结冰能力实验,比例尺均为 10 mm。(a) 抗结冰实验装置示意图;(b)~(j)原始 Al-I 样品和 (k)~(s)超疏水 Al-II 样品表面结冰和防结冰实验过程的对比

Fig. 11 Anti-icing ability test of 7075 aluminum sample, all scales are 10 mm. (a) Schematic of anti-icing test device; comparison of surface freezing and anti-icing processes between (b)~(j) original Al-I sample and (k)~(s) superhydrophobic Al-II sample

### 3.5 抗菌

金属的超疏水表面具有特殊的非润湿性,结合层次结构和较低的表面能在固体表面和液体表面之间捕获空气层,从而有效地抑制细菌对材料的黏附<sup>[49]</sup>。实验以革兰氏阴性大肠杆菌为典型的表面抗菌测试细菌模型,通过激光共聚焦显微镜观察和平板涂布计数测试了铝基超疏水表面的抗菌性能。

利用激光共聚焦显微镜拍摄细菌存活情况及分布图像<sup>[50-51]</sup>,对 Al-I 和 Al-II 两种样品表面的防菌性能进行定性测试。用量筒量取 100 mL 蒸馏水倒入 250 mL 试剂瓶中,用分析电子天平分别称取 2.5 g LB 肉汤培养基加入混匀后,于 121 °C 高温高压蒸汽灭菌锅中灭菌 15 min 后待用。取两支 12 mL 细菌培养管,各加入 6 mL LB 液体培养基,从大肠杆菌固体培养基上挑取单菌落加入液体培养基中,放于恒温振荡器(37 °C, 200 r/min)振荡培养过夜。将 Al-I 和 Al-II 两种样品按照分组放入一次性小皿中,在紫外灯下对样品两面分别照射灭菌 30 min。灭菌后,分别放于 35 mL 磷酸盐缓冲液(PBS)稀释的  $10^8$  CFU/mL 菌液中,于 37 °C 培养箱静置培养 18 h,培养结束后,将样品取出,做死活染色成像。配制染色工作液(1 mL PBS 溶液加入

1  $\mu$ L SYTO-9 和 1  $\mu$ L PI),各取 500  $\mu$ L 染色工作液加至测试样品表面,在 37 °C 下避光染色 15 min。染色完成后,将两种样品测试面放在激光共聚焦显微镜下(600 倍油镜)观察,实验结果如图 12 所示,其中图 12(a)、(c)为 SYTO-9 通道下拍摄的存活在样品表面的细菌分布情况,图 12(b)、(d)为 PI 通道下拍摄的死亡细菌分布情况。可以看出,超疏水 Al-II 样品表面附着的菌株数量明显低于原始 Al-I 样品,说明制备的超疏水样品具有较强的抵抗细菌黏附的能力。

利用平板涂布法对 Al-I 和 Al-II 两种样品表面的杀菌性能进行定量测试<sup>[52-53]</sup>。首先,制备 LB 液体培养基:用量筒量取 100 mL 蒸馏水倒入 250 mL 试剂瓶中,用分析电子天平分别称取 2.5 g LB 肉汤培养基加入混匀后,于 121 °C 高温高压蒸汽灭菌锅中灭菌 15 min 后待用。然后,制备 LB 固体培养基:用量筒量取 100 mL 蒸馏水倒入 250 mL 试剂瓶中,用分析电子天平分别称取 2.5 g LB 肉汤培养基和 1.5 g 琼脂粉,将以上称取试剂加入混匀后,于 121 °C 高温高压蒸汽灭菌锅中灭菌 15 min 备用。待培养基冷却至 40~50 °C 左右,用电动移液器吸取 15 mL 培养基倒入一次性无菌平皿中。取三支



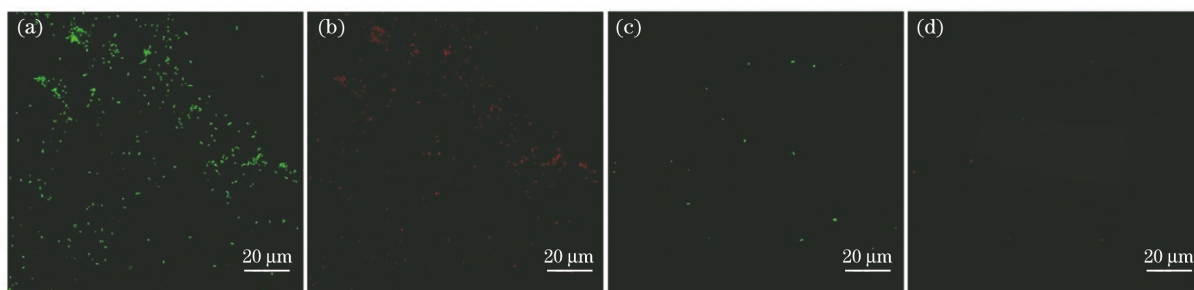


图 12 样品表面大肠杆菌的激光共聚焦显微镜图。Al-I 样品(a)存活细菌分布和(b)死亡细菌分布；Al-II 样品 (c)存活细菌分布和(d)死亡细菌分布

Fig. 12 Laser confocal microscopy of escherichia coli on the sample surface. Distributions of (a) viable bacteria and (b) dead bacteria in Al-I sample; distributions of (c) viable bacteria and (d) dead bacteria in Al-II sample

12 mL 细菌培养管,各加入 6 mL LB 液体培养基,从大肠杆菌固体培养基上挑取单菌落加入液体培养基中,置于恒温振荡器(37 °C, 200 r/min)振荡培养过夜(15 h)。将 Al-I 和 Al-II 两种样品按照分组放入一次性小皿中,在紫外灯下对样品两面分别照射灭菌 30 min。设置实验分组为空白组、Al-I 组和 Al-II 组,用 PBS 溶液将大肠杆菌菌液稀释至  $10^8$  CFU/mL,将样品加入对应编号的锥形瓶中,向锥形瓶中加入 35 mL 稀释后的菌液,将锥形瓶置于恒温培养箱中 37 °C 培养 18 h。培养完成后,用 PBS

将菌液做连续 10 倍稀释( $10^4$ 、 $10^5$ 、 $10^6$  3 个稀释倍数),取 100 μL 稀释液均匀涂布在 LB 固体培养基上,置于 37 °C 恒温培养箱中培养 18 h,取出拍照并记录菌落数。空白组、Al-I 组和 Al-II 组在不同菌液浓度下的菌落分布如图 13 所示,其中对稀释  $10^5$  倍的菌落分布进行菌落计数并计算抑菌率,计算结果如表 2 所示。通过对比可以看出超疏水 Al-II 样品的抑菌率是原始 Al-I 样品的 3.8 倍,由此证明拥有网格状微结构的铝基超疏水表面具有一定的杀菌特性。

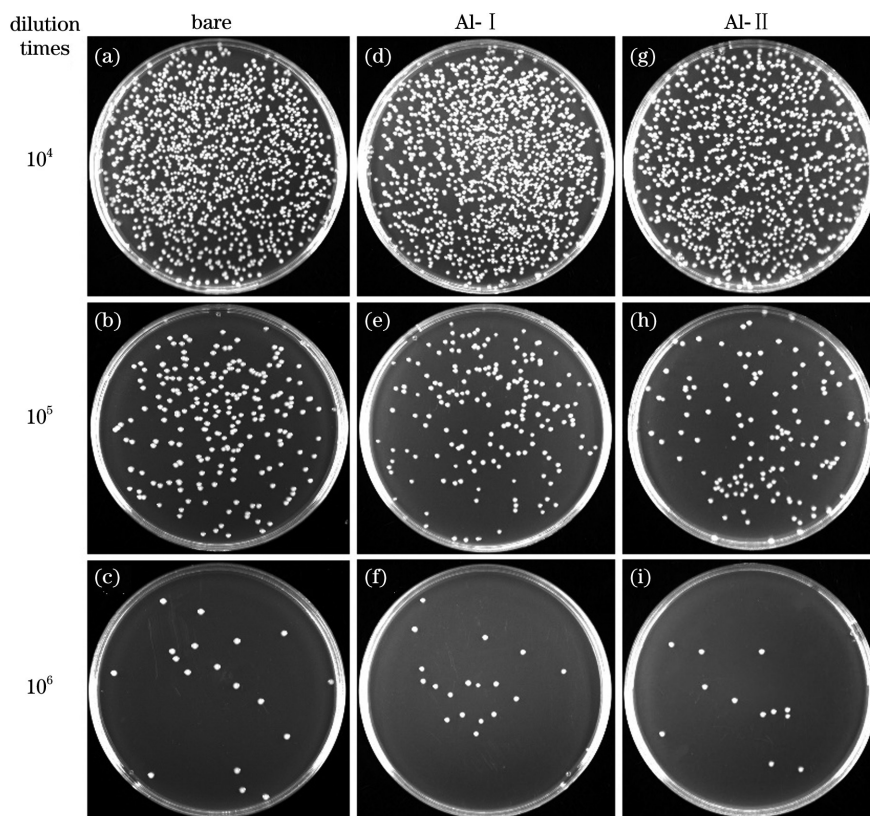


图 13 剩余细菌在不同稀释倍数下的平板涂布菌落数照片。(a)~(c)空白对照组；(d)~(f)原始样品；(g)~(i)超疏水样品

Fig. 13 Colony count of remaining bacteria in plate coating at different dilution ratio. (a)~(c) Bare group; (d)~(f) original sample; (g)~(i) superhydrophobic sample

表 2 菌液稀释  $10^5$  倍后的抑菌情况对比  
Table 2 Comparison of bacterial inhibition after  $10^5$  times dilution

Sample	Concentration of bacteria	Colony count /CFU	Antibacterial rate /%
Bare group	$1.38 \times 10^8$	138	0
Al-I	$1.27 \times 10^8$	127	8.0
Al-II	$9.60 \times 10^7$	96	30.4

## 4 结 论

微夹持器作为微操作系统的末端执行器,在微装配、生物技术和纳米技术等研究领域应用广泛,而传统微夹持器存在诸多问题,例如在多尘和低温环境下执行操作时容易出现吸附杂质、结冰和结霜等问题,在夹取不同对象时,存在磨损或腐蚀等问题,并且其钳口端面一旦受损只能采取整体报废的处理措施,容易造成资源浪费。本实验设计并制作了一种可拆卸式微夹持器,且其夹体的钳口端面具有仿生超疏水结构,很好地解决了传统微夹持器存在的问题。本实验的主要研究内容与创新之处包括:首先,将微夹持器的基体和左、右两个夹体拆分设计,通过螺栓连接基体和夹体,这种设计增加了微夹持器的柔性与灵活性,可以根据不同的夹持对象与工作条件更换相应的夹体,并且当夹体的钳口端面多次使用而受损时,仅需替换夹体部分即可,无需更换整台微夹持器。其次,将激光纹理化的钳口端面经低表面能的硬脂酸溶液浸泡后,获得超疏水特性。该表面拥有的粗糙微结构和较低的表面能有利于在该表面和液体表面之间形成空气层,从而有效地阻止腐蚀性溶液、普通水滴、细菌性溶液等介质与材料表面的接触并抑制液滴的黏附,从而使表面获得自清洁、抗腐蚀、抗结冰、抗结霜等特性,有效提升了微夹持器的使用性能。

## 参 考 文 献

- [1] Sam E K, Sam D K, Lü X M, et al. Recent development in the fabrication of self-healing superhydrophobic surfaces[J]. *Chemical Engineering Journal*, 2019, 373: 531-546.
- [2] Zhan Y L, Ruan M, Li W, et al. Fabrication of anisotropic PTFE superhydrophobic surfaces using laser microprocessing and their self-cleaning and anti-icing behavior[J]. *Colloids and Surfaces A*, 2017, 535: 8-15.
- [3] Pan Q F, Cao Y, Xue W, et al. Picosecond laser-textured stainless steel superhydrophobic surface with an antibacterial adhesion property [J]. *Langmuir*, 2019, 35(35): 11414-11421.
- [4] Latthe S S, Terashima C, Nakata K, et al. Superhydrophobic surfaces developed by mimicking hierarchical surface morphology of lotus leaf [J]. *Molecules*, 2014, 19(4): 4256-4283.
- [5] Bai H, Zhang L, Gu D. Micrometer-sized spherulites as building blocks for lotus leaf-like superhydrophobic coatings[J]. *Applied Surface Science*, 2018, 459: 54-62.
- [6] Tie L, Guo Z G, Liu W M. Anisotropic wetting properties on various shape of parallel grooved microstructure[J]. *Journal of Colloid and Interface Science*, 2015, 453: 142-150.
- [7] Yang L, Shen X D, Yang Q, et al. Fabrication of biomimetic anisotropic super-hydrophobic surface with rice leaf-like structures by femtosecond laser[J]. *Optical Materials*, 2021, 112: 110740.
- [8] Gao F, Yao Y, Wang W, et al. Light-driven transformation of bio-inspired superhydrophobic structure via reconfigurable PAzoMA microarrays: from lotus leaf to rice leaf [J]. *Macromolecules*, 2018, 51(7): 2742-2749.
- [9] May R M, Magin C M, Mann E E, et al. An engineered micropattern to reduce bacterial colonization, platelet adhesion and fibrin sheath formation for improved biocompatibility of central venous catheters [J]. *Clinical and Translational Medicine*, 2015, 4(1): e9.
- [10] Liu Y B, Gu H M, Jia Y, et al. Design and preparation of biomimetic polydimethylsiloxane (PDMS) films with superhydrophobic, self-healing and drag reduction properties via replication of shark skin and SI-ATRP [J]. *Chemical Engineering Journal*, 2019, 356: 318-328.
- [11] Bixler G D, Bhushan B. Bioinspired rice leaf and butterfly wing surface structures combining shark skin and lotus effects[J]. *Soft Matter*, 2012, 8(44): 11271.
- [12] Ivanova E P, Hasan J, Webb H K, et al. Bactericidal activity of black silicon[J]. *Nature Communications*, 2013, 4: 2838.
- [13] Ivanova E P, Hasan J, Webb H K, et al. Natural bactericidal surfaces: mechanical rupture of pseudomonas aeruginosa cells by cicada wings [J]. *Small*, 2012, 8(16): 2489-2494.
- [14] Nguyen S H T, Webb H K, Hasan J, et al. Dual role of outer epicuticular lipids in determining the wettability of dragonfly wings [J]. *Colloids and*

- Surfaces B, 2013, 106: 126-134.
- [15] Li J, Wang W J, Mei X S, et al. Designable ultratransparent and superhydrophobic surface of embedded artificial compound eye with extremely low adhesion[J]. ACS Applied Materials & Interfaces, 2020, 12(47): 53557-53567.
- [16] Li J, Wang W J, Zhu R X, et al. Superhydrophobic artificial compound eye with high transparency[J]. ACS Applied Materials & Interfaces, 2021, 13(29): 35026-35037.
- [17] Yu C M, Sasic S, Liu K, et al. Nature-inspired self-cleaning surfaces: mechanisms, modelling, and manufacturing [J]. Chemical Engineering Research and Design, 2020, 155: 48-65.
- [18] Liu K S, Jiang L. Bio-inspired self-cleaning surfaces [J]. Annual Review of Materials Research, 2012, 42: 231-263.
- [19] Maurer J A, Miller M J, Bartolucci S F. Self-cleaning superhydrophobic nanocomposite surfaces generated by laser pulse heating [J]. Journal of Colloid and Interface Science, 2018, 524: 204-208.
- [20] Gu Y Q, Zhang W Q, Mou J G, et al. Research progress of biomimetic superhydrophobic surface characteristics, fabrication, and application [J]. Advances in Mechanical Engineering, 2017, 9(12): 1-13.
- [21] Xie H, Régnier S. Development of a flexible robotic system for multiscale applications of micro/nanoscale manipulation and assembly[J]. IEEE/ASME Transactions on Mechatronics, 2011, 16(2): 266-276.
- [22] Long Z L, Zhang J G, Liu Y C, et al. Dynamics modeling and residual vibration control of a piezoelectric gripper during wire bonding[J]. IEEE Transactions on Components, Packaging and Manufacturing Technology, 2017, 7(12): 2045-2056.
- [23] Zimmermann S, Tiemerding T, Fatikow S. Automated robotic manipulation of individual colloidal particles using vision-based control [J]. IEEE/ASME Transactions on Mechatronics, 2015, 20(5): 2031-2038.
- [24] Wang F J, Liang C M, Tian Y L, et al. Design and control of a compliant microgripper with a large amplification ratio for high-speed micro manipulation [J]. IEEE/ASME Transactions on Mechatronics, 2016, 21(3): 1262-1271.
- [25] Wang R Z, Zhang X M. Parameters optimization and experiment of a planar parallel 3-DOF nanomanipulation system[J]. IEEE Transactions on Industrial Electronics, 2018, 65(3): 2388-2397.
- [26] Kim B S, Park J S, Kang B H, et al. Fabrication and property analysis of a MEMS micro-gripper for robotic micro-manipulation[J]. Robotics and Computer-Integrated Manufacturing, 2012, 28(1): 50-56.
- [27] Han K, Lee S H, Moon W, et al. Design and fabrication of the micro-gripper for manipulating the cell[J]. Integrated Ferroelectrics, 2007, 89(1): 77-86.
- [28] Shao G B, Ware H O T, Huang J G, et al. 3D printed magnetically-actuating micro-gripper operates in air and water[J]. Additive Manufacturing, 2021, 38: 101834.
- [29] Gaafar E, Member I S, Zarog M. A low-stress and low temperature gradient microgripper for biomedical applications [J]. Microsystem Technologies, 2017, 23(12): 5415-5422.
- [30] Rundla V, Khunteta A. A novel design of micro-gripper with enhanced displacement [C] // 2016 International Conference on Advances in Computing, Communications and Informatics ( ICACCI ), September 21-24, 2016, Jaipur, India. New York: IEEE Press, 2016: 1250-1254.
- [31] Nah S K, Zhong Z W. A microgripper using piezoelectric actuation for micro-object manipulation [J]. Sensors and Actuators A, 2007, 133(1): 218-224.
- [32] Feng L B, Yan Z N, Shi X T, et al. Anti-icing/frosting and self-cleaning performance of superhydrophobic aluminum alloys [J]. Applied Physics A, 2018, 124(2): 1-14.
- [33] Li Q Q, Bao X G, Sun J E, et al. Fabrication of superhydrophobic composite coating of hydroxyapatite/stearic acid on magnesium alloy and its corrosion resistance, antibacterial adhesion [J]. Journal of Materials Science, 2021, 56(8): 5233-5249.
- [34] Huang Y, Sarkar D K, Chen X G. Superhydrophobic aluminum alloy surfaces prepared by chemical etching process and their corrosion resistance properties[J]. Applied Surface Science, 2015, 356: 1012-1024.
- [35] Yang Z, Liu X P, Tian Y L. Fabrication of superhydrophobic nickel film on copper substrate with improved corrosion inhibition by electrodeposition process[J]. Colloids and Surfaces A, 2019, 560: 205-212.
- [36] Wang M, Zhang D W, Yang Z, et al. A contrastive investigation on the anticorrosive performance of stearic acid and fluoroalkylsilane-modified superhydrophobic surface in salt, alkali, and acid solution [J]. Langmuir, 2020, 36(34): 10279-10292.

- [37] 王青华, 王慧鑫, 王占栋, 等. 高效纳秒激光多功能表面制备及抗腐蚀性研究[J]. 中国激光, 2021, 48(14): 1402018.  
Wang Q H, Wang H X, Wang Z D, et al. Highly efficient nanosecond laser-based multifunctional surface fabrication and corrosion resistance performance[J]. Chinese Journal of Lasers, 2021, 48(14): 1402018.
- [38] Vazirinasab E, Jafari R, Momen G. Application of superhydrophobic coatings as a corrosion barrier: a review[J]. Surface and Coatings Technology, 2018, 341: 40-56.
- [39] Yao X, Song Y L, Jiang L. Applications of bio-inspired special wettable surfaces [J]. Advanced Materials, 2011, 23(6): 719-734.
- [40] Wang D H, Sun Q Q, Hokkanen M J, et al. Design of robust superhydrophobic surfaces [J]. Nature, 2020, 582(7810): 55-59.
- [41] Long Y F, Yin X X, Mu P, et al. Slippery liquid-infused porous surface (SLIPS) with superior liquid repellency, anti-corrosion, anti-icing and intensified durability for protecting substrates [J]. Chemical Engineering Journal, 2020, 401: 126137.
- [42] 江国琛, 潘瑞, 陈昶昊, 等. 超快激光制备水面减阻微纳结构及其耐腐蚀性研究[J]. 中国激光, 2020, 47(8): 0802005.  
Jiang G C, Pan R, Chen C H, et al. Ultrafast laser fabricated drag reduction micro-nano structures and their corrosion resistance [J]. Chinese Journal of Lasers, 2020, 47(8): 0802005.
- [43] Zhao X, Wei J F, Li B C, et al. A self-healing superamphiphobic coating for efficient corrosion protection of magnesium alloy[J]. Journal of Colloid and Interface Science, 2020, 575: 140-149.
- [44] He Z H, Zeng Y W, Zhou M M, et al. Superhydrophobic films with enhanced corrosion resistance and self-cleaning performance on an Al alloy[J]. Langmuir, 2021, 37(1): 524-541.
- [45] Yang Z, Liu X P, Tian Y L. Novel metal-organic super-hydrophobic surface fabricated by nanosecond laser irradiation in solution[J]. Colloids and Surfaces A, 2020, 587: 124343.
- [46] Zang D M, Xun X W, Gu Z D, et al. Fabrication of superhydrophobic self-cleaning manganese dioxide coatings on Mg alloys inspired by lotus flower [J]. Ceramics International, 2020, 46(12): 20328-20334.
- [47] Yang C J, Chao J Q, Zhang J C, et al. Functionalized CFRP surface with water-repellence, self-cleaning and anti-icing properties [J]. Colloids and Surfaces A, 2020, 586: 124278.
- [48] 潘瑞, 张红军, 钟敏霖. 三级微纳超疏水表面的超快激光复合制备及防除冰性能研究[J]. 中国激光, 2021, 48(2): 0202009.  
Pan R, Zhang H J, Zhong M L. Ultrafast laser hybrid fabrication and ice-resistance performance of a triple-scale micro/nano superhydrophobic surface[J]. Chinese Journal of Lasers, 2021, 48(2): 0202009.
- [49] Zhang X X, Wang L, Levänen E. Superhydrophobic surfaces for the reduction of bacterial adhesion [J]. RSC Advances, 2013, 3(30): 12003-12020.
- [50] Guerreiro-Tanomaru J M, Nascimento C A, Faria-Júnior N B, et al. Antibiofilm activity of irrigating solutions associated with cetrimide. Confocal laser scanning microscopy [J]. International Endodontic Journal, 2014, 47(11): 1058-1063.
- [51] Yan J, Bassler B L. Surviving as a community: antibiotic tolerance and persistence in bacterial biofilms[J]. Cell Host & Microbe, 2019, 26(1): 15-21.
- [52] Niu X M, Wan S Q, Rong X N, et al. Facile fabrication of povidone iodine-embedded polytetrafluoroethylene superhydrophobic films with improved antiadhesive and bactericidal properties in bacterial environments[J]. Macromolecular Materials and Engineering, 2021, 306(9): 2100193.
- [53] Ishwarya R, Vaseeharan B, Kalyani S, et al. Facile green synthesis of zinc oxide nanoparticles using Ulva lactuca seaweed extract and evaluation of their photocatalytic, antibiofilm and insecticidal activity [J]. Journal of Photochemistry and Photobiology B, 2018, 178: 249-258.

# Application of Bionic Superhydrophobic Surface in Jaw End Face of Microgripper

Yang Chengjuan<sup>1,2</sup>, Yang Xue<sup>1,2\*</sup>, Wang Meng<sup>1,2</sup>, Wang Fujun<sup>1,2</sup>, Shi Beichao<sup>1,2</sup>,  
Zhu Xinyao<sup>1,2</sup>

<sup>1</sup> School of Mechanical Engineering, Tianjin University, Tianjin 300072, China;

<sup>2</sup> Key Laboratory of Mechanism Theory and Equipment Design, Ministry of Education, School of Mechanical Engineering, Tianjin University, Tianjin 300072, China

## Abstract

**Objective** A microgripper is an essential part of the micromanipulation system. As the end effector of the microoperating system, the jaw end face of the microgripper is prone to wear, adsorption of impurities, ice, or frost during operation. Most traditional microgrippers are integrally machined, and the overall replacement will result in wasted resources. This study reports a detachable microgripper with superhydrophobic properties. First, a rough microstructure was machined on the end face of the jaws where the operation is performed using a nanosecond laser with a central wavelength of 1064 nm. Then, they are modified by immersing them in a nontoxic stearic acid solution. Thus, a bionic superhydrophobic surface is obtained. This surface has excellent corrosion resistance, self-cleaning, antiicing, and antibacterial properties. X-ray photoelectron spectroscopy (XPS) technique is employed to analyze the chemical composition of the pristine aluminum (Al-I) and superhydrophobic aluminum (Al-II) surfaces; the corrosion resistance of both surfaces in acid, salt, and alkali environments is tested using electrochemical experiments. Further, the antifouling, antifreezing, and antibacterial properties of both surfaces are tested using self-cleaning, antiicing, and antibacterial experiments. We expect that our basic strategies and findings will enhance the performance and extend the service life of the microgrippers.

**Methods** Because the microgripper is made of 7075 space aluminum used to facilitate later observation, testing, and analysis, a 7075 aluminum sample with size and thickness of 10 mm × 10 mm and 1 mm, respectively, is used for the test instead of the end face of the jaws. First, a nanosecond laser is used to etch a grid-like microstructure on the surface of the sample, and then it is immersed in a nontoxic stearic acid solution with a concentration of 0.05 mol/L for 30 min to reduce the surface free energy. Further, it is removed and placed in a drying oven at 60 °C for 1 h. The sample surface will acquire the expected superhydrophobic properties using this procedure. According to the functional requirements of the microgripper, the prepared superhydrophobic sample surfaces are analyzed for surface composition and tested for corrosion resistance, self-cleaning, antiicing, and antibacterial properties. The chemical composition of Al-I and Al-II surfaces is detected using the XPS technique. Further, the morphology of the sample surfaces before and after corrosion by acid, salt, and alkali is characterized using scanning electron microscopy. The antiicing and self-cleaning performance of the sample surfaces are evaluated using an environmental test chamber and self-designed self-cleaning experiments. The bacterial distribution and survival status of the sample surfaces are characterized using laser confocal microscopy, and the antibacterial performance is characterized using plate coating experiments to calculate the bacterial inhibition rate.

**Results and Discussions** The lattice-like microstructures obtained from the sample surface preparation have high superhydrophobicity with average contact and rolling angles of 156.7° and 1.088°, respectively. The XPS test results show that the surface of both samples mainly contains C, O, and Al elements. After laser irradiation, the generated Al<sub>2</sub>O<sub>3</sub> on the surface caused the O atomic number fraction to increase by 24.51%. The C 1s high-resolution spectra of the superhydrophobic samples exhibit a significant increase in C atomic number fraction following the stearic acid modification treatment, indicating that stearic acid reacted with the surface Al to form low surface energy aluminum stearate during the chemical modification process. The C—C (H) content is as high as 82.81%, occupying the strongest peak, which indicates that the long-chain molecules of stearic acid have successfully adhered to the surface of the Al-II sample in the form of aluminum stearate (Fig. 5). Electrochemical experiments and SEM results show that the corrosion resistance of the superhydrophobic surface in a salt solution is better than its resistance to acids and bases; the total impedance modulus of superhydrophobic Al-II sample is better than that of pristine Al-I sample. This implies that the superhydrophobic surface with a rough microstructure can significantly enhance the corrosion

inhibition of aluminum materials (Figs. 6–8, Table 1). The self-cleaning test results show that the droplets can effectively remove the impurities from the surface of the Al- II sample, indicating that the superhydrophobic surface has a good self-cleaning ability (Fig. 10). The results of the twenty-minute antiicing experiments show that the Al- II sample has excellent superhydrophobicity with low adhesion ability and no significant icing occurred during the test, whereas the adhering ice layer on the surface of the Al- I sample has a mass of 1.283 g and shows poor antiicing performance in the cryogenic environment (Fig. 11). The results of laser confocal microscope characterization in the antibacterial experiment show that the number of strains adhering to the surface of the Al- II sample is significantly lower than that of the Al- I sample, indicating that the prepared superhydrophobic sample has a strong resistance to bacterial adhesion (Fig. 12). Further, the results of the plate-coating experiment show that the antibacterial rate of the Al- II sample is 3.8 times higher than that of the original Al- I sample, which proves that the aluminum-based superhydrophobic surface with lattice-like microstructure has certain bactericidal properties (Table 2).

**Conclusions** In this study, we design and construct a detachable microgripper with a bionic superhydrophobic structure in the jaw end of the gripper body, which addresses several problems of the traditional microgripper. The main research contents and innovations are as follows: 1) the microgripper's base body and the left and right clamping bodies are designed separately and connected by bolts. This design increases the flexibility of the microgripper, which can replace the corresponding body based on different clamping objects and working conditions. When the jaw end face is damaged by repeated use, it is unnecessary to replace the whole microgripper; however, only the body part can be replaced. 2) The laser-textured jaw end faces are soaked in a low surface energy stearic acid solution to obtain superhydrophobic properties. The surface obtained through this method has a rough microstructure and low surface energy, thus forming an air layer between the material and the liquid; it effectively prevents the contact of the material surface with corrosive solutions, common water droplets, and bacterial solutions inhibiting the adhesion of droplets. This enables the jaw end faces to acquire self-cleaning, anticorrosion, antiicing, and antifrost properties, thus effectively enhancing the clamping performance of the microgripper.

**Key words** laser technique; surface processing; bionic superhydrophobic surface; microgripper; corrosion resistance; self-cleaning; antiicing; antibacterial